Inorganic Chemistry
Article
pubs.acs.org/IC

# Single-Molecule Magnetism in a Family of $\{Co^{III}{}_2Dy^{III}{}_2\}$ Butterfly Complexes: Effects of Ligand Replacement on the Dynamics of Magnetic Relaxation

Stuart K. Langley,[†] Liviu Ungur,[‡] Nicholas F. Chilton,[§] Boujemaa Moubaraki,[†] Liviu F. Chibotaru,*[,‡] and Keith S. Murray*[,†]

[†]School of Chemistry, Monash University, Clayton, Victoria 3800, Australia

[‡]Theory of Nanomaterials Group and INPAC—Institute of Nanoscale Physics and Chemistry, Katholieke Universiteit Leuven, Celestijnenlaan 200F, 3001 Heverlee, Belgium

[§]School of Chemistry, The University of Manchester, Manchester M13 9PL, U.K.

S *Supporting Information*

**ABSTRACT:** The synthesis and structural characterization of four related heterometallic complexes of formulas $[Dy^{III}{}_2Co^{III}{}_2(OMe)_2(teaH)_2(O_2CPh)_4(MeOH)_4](NO_3)_2\cdot MeOH\cdot H_2O$ (**1a**) and $[Dy^{III}{}_2Co^{III}{}_2(OMe)_2(teaH)_2(O_2CPh)_4(MeOH)_2(NO_3)_2]\cdot MeOH\cdot H_2O$ (**1b**), $[Dy^{III}{}_2Co^{III}{}_2(OMe)_2(dea)_2(O_2CPh)_4(MeOH)_4](NO_3)_2$ (**2**), $[Dy^{III}{}_2Co^{III}{}_2(OMe)_2(mdea)_2(O_2CPh)_4(NO_3)_2]$ (**3**), and $[Dy^{III}{}_2Co^{III}{}_2(OMe)_2(bdea)_2(O_2CPh)_4(MeOH)_4](NO_3)_2\cdot 0.5MeOH\cdot H_2O$ (**4a**) and $[Dy^{III}{}_2Co^{III}{}_2(OMe)_2(bdea)_2(O_2CPh)_4(MeOH)_2(NO_3)_2]\cdot MeOH\cdot 1.5H_2O$ (**4b**) are reported ($teaH_3$ = triethanolamine, $deaH_2$ = diethanolamine, $mdeaH_2$ = *N*-methyldiethanolamine, and $bdeaH_2$ = *N*-n-butyldiethanolamine). Compounds **1** (≡ **1a** and **1b**) and **4** (≡ **4a** and **4b**) both display two unique molecules within the same crystal and all compounds display a butterfly type core, with the $Dy^{III}$ ions occupying the central body positions and the diamagnetic $Co^{III}$ ions the outer wing-tip sites. Compounds **1**−**4** were investigated via direct current and alternating current magnetic susceptibility measurements, and it was found that each complex displayed single-molecule magnet (SMM) behavior. All four compounds display unique coordination and geometric environments around the $Dy^{III}$ ions and it was found that each displays a different anisotropy barrier. *Ab initio* calculations were performed on **1**−**4** and these determined the low lying electronic structure of each $Dy^{III}$ ion and the magnetic interactions for each cluster. It was found that there was a strong correlation between the calculated energy gap between the ground and first excited states of the single-ion ligand-field split $Dy^{III}$ levels and the experimentally observed anisotropy barrier. Furthermore, the transverse *g* factors found for the $Dy^{III}$ ions, defining the tunnelling rates within the ground Kramers doublets, are largest for **1**, which agrees with the experimental observation of the shortest relaxation time in the high-temperature domain for this complex. The magnetic exchange between the $Dy^{III}$ ions revealed overall antiferromagnetic interactions for each compound, derived from the dominant dipolar exchange resulting in nonmagnetic ground states for **1**−**4**. The diamagnetic ground states coupled with small tunneling gaps resulted in quantum tunneling time scales at zero field of between 0.1 and >1.5 s.

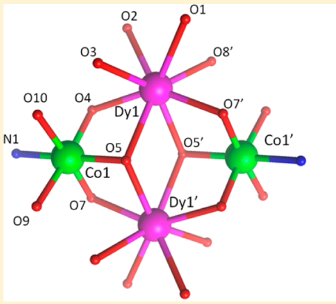

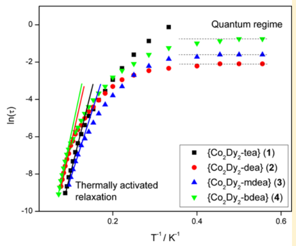

## ■ INTRODUCTION

Since the discovery that a dodecanuclear manganese complex; $[Mn_{12}O_{12}(O_2CR)_{16}(H_2O)_4]$ displays slow magnetic relaxation, numerous coordination complexes have since been isolated which display so-called single-molecule magnet (SMM) behavior.[1] This property is brought about via an anisotropic energy barrier ($U_{eff}$) blocking the magnetization with a specific orientation at low temperatures. Magnetic hysteresis of purely molecular origin is therefore observable in the majority of such cases, at low enough temperatures, and these molecules may potentially be used in future high density data storage devices and for quantum information processing.[2] Many of the early reported SMMs were based on polynuclear 3d complexes, with the majority containing manganese.[3] In more recent years the discovery of single ion lanthanide complexes exhibiting this effect, in particular a family of $\{Ln(pc)_2\}^-$ (Pc = dianion of phthalocyanine) compounds with extremely large energy barriers to magnetization reversal, has revitalized the search for high(er) temperature SMMs.[4] Several such mono- and polynuclear lanthanide species have since been reported displaying very large energy barriers to magnetic reorientation compared to their transition metal counterparts;[5] however, a poor understanding of the relaxation mechanism and the problem of fast quantum tunnelling of magnetization (QTM) are important challenges to overcome at the present time.

**Received:** December 2, 2013
**Published:** April 21, 2014

Continued research into the understanding of the relaxation mechanism is key to developing lanthanide-based SMMs with longer relaxation times at higher temperatures. One key pathway toward this goal lies in the use of *ab initio* calculations. Such calculations have proven valuable towards understanding the complicated nature of anisotropic magnetism in lanthanide molecular complexes.[6] These calculations can accurately determine the low lying electronic structure of the individual ions, which are often difficult to access experimentally, and they are also able to elucidate the Ln···Ln exchange interactions in polynuclear systems.

Recently we reported the crystal structure of two near identical 3d/4f complexes which consist of two dinuclear $Dy^{III}$ species that cocrystallize within the same crystal, each encapsulated within two diamagnetic $Co^{III}$ ions and several organic bridging ligands.[7] The complexes $[Dy^{III}_2Co^{III}_2(OMe)_2(teaH)_2(O_2CPh)_4(MeOH)_4](NO_3)_2\cdot MeOH\cdot H_2O$ (**1a**) and $[Dy^{III}_2Co^{III}_2(OMe)_2(teaH)_2(O_2CPh)_4(MeOH)_2(NO_3)_2]\cdot MeOH\cdot H_2O$ (**1b**) ($teaH_3$ = triethanolamine) are thus heterometallic 3d/4f clusters, but magnetically can be considered as dinuclear $Dy^{III}$ units, due to the low spin $Co^{III}$ $d^6$ ions. From alternating current (ac) magnetic susceptibility experiments we observed SMM behavior with a substantial energy barrier (~61 $cm^{-1}$) to magnetic reversal and a relatively slow zero-field QTM time for a lanthanide dimer (>1.5 s), which generally is found to be on the millisecond time scale. It was found via *ab initio* calculations, that the QTM in **1** (**1** ≡ **1a** and **1b**) is efficiently suppressed due to the small tunnelling gap of the ground exchange doublet which is of the order of $10^{-6}$ $cm^{-1}$. This is due to the non-Kramers nature of the coupled system and the weak antiferromagnetic interactions between the $Dy^{III}$ ions, resulting in a nonmagnetic ground state. This results in a vanishing local transverse field as the temperature tends to zero, thus removing this contribution to the QTM. This was confirmed experimentally via dilution experiments in which we were able to isolate the "magnetically monomeric" $\{Dy^{III}Y^{III}Co^{III}_2\}$ species, which resulted in the QTM being "turned back on," where fast tunnelling was observed at zero field, with a characteristic time of 0.15 ms.[7]

To gain a better understanding of the relaxation mechanism(s) in lanthanide systems we have continued to study this particular system by careful variation of the reaction conditions to isolate chemical/structural variants of compound **1**. It was found that the use of three amine-based diol ligands—diethanolamine ($deaH_2$), *N*-methyldiethanolamine ($mdeaH_2$), and *N*-n-butyldiethanolamine ($bdeaH_2$)—substituted in place of triethanolamine ($teaH_3$), in conjunction with benzoic acid, allowed us access to several related complexes. The molecular structures of the proligands are shown in Scheme 1.

The use of $deaH_2$ resulted in the isolation of the cationic form of compound **1**, of formula $[Dy^{III}_2Co^{III}_2(OMe)_2(dea)_2(O_2CPh)_4(MeOH)_4](NO_3)_2$, (**2**). The use of $mdeaH_2$ resulted in a variation of both **1** and **2**, with one unique structure found in the asymmetric unit, as with **2**, but with the coordination environment around the $Dy^{III}$ centers differing from those previously seen. This neutral complex has the formula $[Dy^{III}_2Co^{III}_2(OMe)_2(mdea)_2(O_2CPh)_4(NO_3)_2]$ (**3**). The reaction utilizing $bdeaH_2$ resulted in the isolation of two unique complexes in the same crystal of formula $[Dy^{III}_2Co^{III}_2(OMe)_2(bdea)_2(O_2CPh)_4(MeOH)_4](NO_3)_2\cdot 0.5MeOH\cdot H_2O$ (**4a**) and $[Dy^{III}_2Co^{III}_2(OMe)_2(bdea)_2(O_2CPh)_4(MeOH)_2(NO_3)_2]\cdot MeOH\cdot 1.5H_2O$ (**4b**), (**4** ≡ **4a** and **4b**), which are structurally similar to those in **1**. Each dysprosium complex, **1**–**4**, behaves as a SMM with a large anisotropic energy barrier, and, although similar in structure, they possess subtly different coordination environments around the $Dy^{III}$ ions. The resulting dynamic (ac) magnetic behavior for each complex is unique and thus these systems are ideal for exploring the factors that affect the anisotropy barrier and/or the relaxation mechanism in lanthanide SMMs.

**Scheme 1. Proligands Used towards the Synthesis of Complexes 1–4**

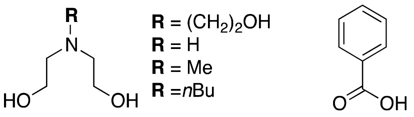

To understand the differences between the magnetization dynamics of **1**–**4**, accurate determination of the electronic structure on the individual metal ions, alongside the magnetic coupling between all metal sites, is required. Fragment *ab initio* calculations of CASSCF/RASSI/SINGLE_ANISO type have proved useful and reliable in the determination of local electronic and magnetic properties of individual lanthanide centers.[8−10] In the second step of the theoretical analysis, magnetic interaction, exchange spectrum and all magnetic properties of each polynuclear system were computed on the basis of fragment *ab initio* results, within the POLY_ANISO routine.[11,12] This information can then be used to interpret the magnetization dynamics of the compounds by employing the concept of magnetic axiality.[13−15]

## ■ EXPERIMENTAL SECTION

**General Information.** All reactions were carried out under aerobic conditions. Chemicals and solvents were obtained from commercial sources and used without further purification. Elemental analyses (C, H, N) were carried out by Campbell Microanalytical Laboratory, University of Otago, Dunedin, New Zealand. IR spectra were recorded on a Bruker Equinox 55 spectrometer with an ATR sampler provided by Specac Inc. and the samples were run neat. The synthesis of compound **1** was as previously reported.[7]

*Synthesis of* $[Dy^{III}_2Co^{III}_2(OMe)_2(dea)_2(O_2CPh)_4(MeOH)_4](NO_3)_2$ (**2**). $Co(NO_3)_2\cdot 6H_2O$ (0.29 g, 1 mmol) and $Dy(NO_3)_3\cdot 6H_2O$ (0.45 g, 1 mmol) were dissolved in MeCN (20 mL), followed by the addition of diethanolamine (0.10 mL, 1 mmol), benzoic acid (0.12 g, 1 mmol), and triethylamine (0.55 mL, 4 mmol) to give a purple solution. This was stirred for 6 h, after which the MeCN was removed and the residue redissolved in MeOH (15 mL), which was allowed to evaporate slowly. Within 2–3 d, purple crystals of **2** appear, in approximate yield of 42%. Anal. Calculated (found) for **2**: $Co_2Dy_2C_{42}H_{60}O_{24}N_4$: C, 34.84 (34.60); H, 4.18 (4.32); N, 3.87 (3.74)%. Selected IR data ATR ($cm^{-1}$): 1595s, 1558s, 1475s, 1446w, 1391s, 1304s, 1175w, 1158w, 1097w, 1075w, 1027w, 926w, 828w, 758w, 720w, 687w.

*Synthesis of* $[Dy^{III}_2Co^{III}_2(OMe)_2(mdea)_2(O_2CPh)_4(NO_3)_2]$ (**3**). As with **2** but *N*-methydiethanolamine (0.12 mL, 1 mmol) was used in place of diethanolamine. Within 2–3 d, purple crystals of **3** appear, in approximate yield of 51%. Anal. Calculated (found) for **3**: $Co_2Dy_2C_{40}H_{48}O_{20}N_4$: C, 35.65 (35.60); H, 3.59 (3.65); N, 4.16 (4.14)%. Selected IR data ATR ($cm^{-1}$): 1596s, 1558s, 1474s, 1389s, 1294m, 1176w, 1156w, 1085w, 1068w, 1022w, 1008w, 940w, 911w, 845w, 828w, 815w, 760w, 738w, 714w, 687w.

*Synthesis of* $[Dy^{III}_2Co^{III}_2(OMe)_2(bdea)_2(O_2CPh)_4(MeOH)_4](NO_3)_2\cdot 0.5MeOH\cdot H_2O$ (**4a**) *and* $[Dy^{III}_2Co^{III}_2(OMe)_2(bdea)_2(O_2CPh)_4(MeOH)_2(NO_3)_2]\cdot MeOH\cdot 1.5H_2O$ (**4b**). As with **2** but *N*-n-butyldiethanolamine (0.16 mL, 1 mmol) was used in place of diethanolamine. Within 2–3 d, blue/purple crystals of **4** appear, in

Table 1. Crystallographic Data for Compounds 1−4

| | 1 | 2 | 3 | 4 |
|---|---|---|---|---|
| formula$^{a,b}$ | $Co_2Dy_2C_{46}H_{70}O_{27}N_4$ | $Co_2Dy_2C_{42}H_{60}O_{24}N_4$ | $Co_2Dy_2C_{40}H_{48}O_{20}N_4$ | $Co_2Dy_2C_{49.75}H_{77.25}O_{25}N_4$ |
| M, g mol$^{-1}$ | 1553.90 | 1447.8 | 1347.68 | 1574.25 |
| crystal system | tetragonal | monoclinic | monoclinic | monoclinic |
| space group | $I4_1/a$ | $P2_1/n$ | $P2_1/n$ | $P2_1/n$ |
| $a$/Å | 40.986(6) | 8.1910(16) | 7.8200(16) | 16.1436(6) |
| $b$/Å | 40.986(6) | 17.672(4) | 17.220(3) | 23.2605(8) |
| $c$/Å | 15.985(3) | 17.370(4) | 17.270(4) | 19.2339(6) |
| $\alpha$/deg | 90 | 90 | 90 | 90 |
| $\beta$/deg | 90 | 97.10(3) | 92.00(3) | 114.6050(10) |
| $\gamma$/deg | 90 | 90 | 90 | 90 |
| V/Å$^3$ | 26852(9) | 2495.1(10) | 2324.2(8) | 6566.7(4) |
| $T$/K | 100(2) | 100(2) | 100(2) | 123(2) |
| $Z$ | 16 | 2 | 2 | 4 |
| $\rho_{calc}$ [g cm$^{-3}$] | 1.535 | 1.927 | 1.926 | 2.822 |
| $\lambda^c$/Å | 0.710 70 | 0.710 70 | 0.710 70 | 0.710 73 |
| data measured | 174 458 | 29 963 | 37 270 | 41 472 |
| ind. reflns | 11 791 | 4373 | 5311 | 14 438 |
| $R_{int}$ | 0.0419 | 0.0291 | 0.0282 | 0.0465 |
| reflns with $I$ ($I > 2\sigma(I)$) | 11 562 | 4190 | 4921 | 10 281 |
| parameters | 787 | 347 | 309 | 817 |
| restraints | 150 | 2 | 0 | 35 |
| $R_1{}^d$ (obs), w$R_2{}^d$ (all) | 0.0543, 0.1572 | 0.0909, 0.2041 | 0.0317, 0.0787 | 0.0477, 0.1319 |
| goodness of fit | 1.049 | 1.122 | 1.058 | 1.040 |
| largest residuals/e Å$^{-3}$ | 2.962, −2.021 | 5.060, −2.915 | 2.558, −0.932 | 5.093, −1.457 |

[a] Including solvate molecules. [b] The average formula of the two molecules for **1** and **4** is given, including solvate molecules. [c] Graphite monochromator. [d] $R_1 = \Sigma||F_0| - |F_c||/\Sigma|F_0|$, $wR_2 = \{\Sigma[w(F_0{}^2 - F_c{}^2)^2]/\Sigma[w(F_0{}^2)^2]\}^{1/2}$.

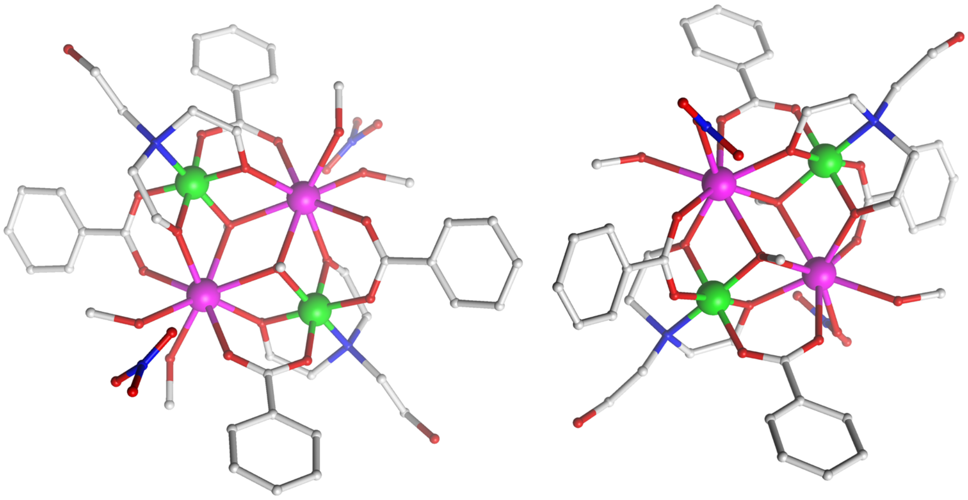

**Figure 1.** The structure of **1a** (left) and **1b** (right) in the crystal.[7] Disordered and H atoms are omitted for clarity. Color scheme; Co$^{III}$, green; Dy$^{III}$, purple; O, red; N, blue; C, light gray.

approximate yield of 68%. Anal. Calculated (found) for **4**: $Co_2Dy_2C_{49.75}H_{75}O_{25}N_4$: C, 38.13 (38.20); H, 4.80 (4.62); N, 3.56 (3.69)%. Selected IR data ATR (cm$^{-1}$): 1595s, 1557s, 1474s, 1447w, 1391s, 1304s, 1175w, 1159w, 1096w, 1075w, 1026w, 926w, 828w, 758w, 720w, 687w.

**X-ray Crystallography.** X-ray measurements for **1**−**3** were performed at 100(2) K at the Australian synchrotron MX1 beamline. The data collection and integration were performed within Blu-Ice[16] and XDS[17] software programs. Compound **4** was measured using a Bruker Smart Apex X8 diffractometer with Mo K$\alpha$ radiation. The data collection and integration were performed within SMART and SAINT + software programs, and corrected for absorption using the Bruker SADABS program. Compounds **1**−**4** were all solved by direct methods (SHELXS-97), and refined (SHELXL-97) by full least matrix least-squares on all $F^2$ data.[18] Crystallographic data and refinement parameters for **1**−**4** are summarized in Table 1. Crystallographic details are available in the Supporting Information in CIF format.

**Magnetic Measurements.** The magnetic susceptibility measurements were carried out using a Quantum Design SQUID magnetometer MPMS-XL 7 operating between 1.8 and 300 K, with direct current (dc)-applied fields ranging from 0−5 T. Microcrystalline samples were dispersed in Vaseline to avoid torquing of the crystallites. The sample mulls were contained in a calibrated gelatin capsule held at the center of a drinking straw that was fixed at the end of the sample rod. Susceptibility measurements (ac) were carried out under an oscillating ac field of 3.5 Oe and frequencies ranging from 0.1 to 1500 Hz.

## ■ RESULTS AND DISCUSSION

**Structural Descriptions.** *$[Dy^{III}_2Co^{III}_2(OMe)_2(teaH)_2(O_2CPh)_4(MeOH)_4](NO_3)_2 \cdot MeOH \cdot H_2O$ (**1a**) and $[Dy^{III}_2Co^{III}_2(OMe)_2(teaH)_2(O_2CPh)_4(MeOH)_2(NO_3)_2] \cdot MeOH \cdot H_2O$ (**1b**).* The structure of **1a** and **1b** (Figure 1) which are regarded overall as compound **1** has been described previously.[7] As **1** is the parent compound of which **2**, **3**, and **4** are family members, a brief description of the salient points are given. Complex **1** crystallizes in the tetragonal space group $I4_1/a$ with the asymmetric unit consisting of two similar but unique heterometallic tetranuclear complexes (**1a** and **1b**). Overall both clusters consist of two $Co^{III}$ and two $Dy^{III}$ ions, with the metallic core best described as a planar butterfly motif, with the $Dy^{III}$ ions occupying the body positions and the $Co^{III}$ ions the outer wing-tips. The difference found between the two compounds is minor, with slightly different coordination environments found around the $Dy^{III}$ ions, via the terminal ligands. Complex **1a** displays two terminal MeOH molecules, while **1b** has one MeOH and a $NO_3^-$ coordinated via one O atom, thus **1a** is cationic and **1b** is neutral.

*$[Dy^{III}_2Co^{III}_2(OMe)_2(dea)_2(O_2CPh)_4(MeOH)_4](NO_3)_2$ (**2**).* Upon replacement of the ligand $teaH_3$ by $deaH_2$ and otherwise following the same synthetic procedure used to prepare **1**, we were able to synthesize complex **2**. In this case only one unique structure was found throughout the crystal. Compound **2** (Figure 2, top) crystallizes in the monoclinic space group $P2_1/n$, with the asymmetric unit containing half the cluster, which lies upon an inversion center and a nitrate counterion. The complex is exclusively cationic, as observed with **1a**, with two MeOH ligands terminally coordinating to each $Dy^{III}$ ion, with two nitrate counterions found in the crystal lattice. The isolation of a single complex from a mixture of two different molecules found within the same crystal upon changing the reaction conditions has been observed previously. One such example is that of two iron complexes; $\{Fe_{17}\}$ and $\{Fe_{19}\}$ cocrystallizing together within the same lattice, which was resolved by modifying the bridging ligand used; $H_3$heidi = *N*-2-hydroxyethyl-iminodiacetic acid to $H_3$metheidi = *N*-(1-hydroxymethylethyl)iminodiacetic acid, resulting in the isolation of the $\{Fe_{19}\}$ cluster only.[19] This was found to be the case with **1** versus **2**, namely, using the ligands $teaH_3$ and $deaH_2$, respectively. The metallic core arrangement in **2** is identical to that of **1a**, again displaying a butterfly type motif. The only overall difference is the two doubly deprotonated $deaH^{2-}$ ligands that are now present, both of which display the $\mu_3{:}\eta^2{:}\eta^2{:}\eta^1$ bonding mode. The two $Co^{III}$ ions are six-coordinate with octahedral geometries, with an average $Co-L_{N,O}$ bond length of 1.926 Å. The two $Dy^{III}$ ions are eight coordinate with distorted square antiprismatic geometries, and have an average Dy−O bond length of 2.370 Å. The closest intermolecular Dy···Dy distance is 7.99 Å.

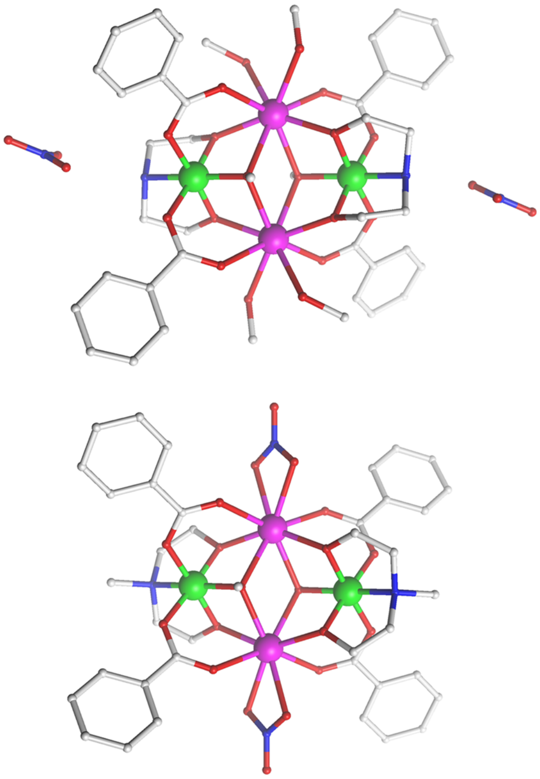

**Figure 2.** The molecular structure of **2** (top) and **3** (bottom). The H atoms are omitted for clarity. The color scheme is as in Figure 1.

*$[Dy^{III}_2Co^{III}_2(OMe)_2(mdea)_2(O_2CPh)_4(NO_3)_2]$ (**3**).* Compound **3** (Figure 2, bottom) crystallizes in the monoclinic space group $P2_1/n$ with the asymmetric unit containing half the cluster which lies upon an inversion center. Again, upon changing the amine polyalcohol ligand, in this case to $mdeaH_2$, we were able to isolate a further variant that differs from both **1** and **2**. In **3**, we again form a planar-butterfly motif with two $Co^{III}$ and two $Dy^{III}$ ions, the difference being the two doubly deprotonated $mdea^{2-}$ ligands which are now present, and more importantly, the coordination environment around the $Dy^{III}$ ions is different. In the case of **1** and **2** we observed two terminal MeOH molecules or one MeOH and one $NO_3^-$ coordinated to the $Dy^{III}$ ion. For **3** we now observe only one chelating $NO_3^-$ ion and the complex is neutral. The two $Co^{III}$ ions are six-coordinate with octahedral geometries, with an average $Co-L_{N,O}$ bond length of 1.919 Å. The two $Dy^{III}$ ions are eight-coordinate with distorted square antiprismatic geometries, with an average Dy−O bond length of 2.358 Å. The closest intermolecular Dy···Dy distance is 7.820 Å.

*$[Dy^{III}_2Co^{III}_2(OMe)_2(bdea)_2(O_2CPh)_4(MeOH)_4](NO_3)_2 \cdot 0.5MeOH \cdot H_2O$ (**4a**) and $[Dy^{III}_2Co^{III}_2(OMe)_2(bdea)_2(O_2CPh)_4(MeOH)_2(NO_3)_2] \cdot MeOH \cdot 1.5H_2O$ (**4b**).* Increasing the size of the alkyl group attached to the N atom of the amine diol ligand by utilizing $bdeaH_2$ resulted in two complexes **4a** and **4b** (**4** ≡ **4a** and **4b**), found within the same crystal (Figure 3). Both compounds consist of two similar but unique tetranuclear complexes and crystallize in the monoclinic space group $P2_1/n$, with the asymmetric unit consisting of one-half of both **4a** and **4b**, with each lying upon an inversion center. Again we observe two unique structures cocrystallizing within the same crystal, with the coordination environments around of the metal ions being identical to that of compound **1**. The only chemical difference when comparing to **1** is the presence of the $bdea^{2-}$ ligand which coordinates via the $\mu_3{:}\eta^2{:}\eta^2{:}\eta^1$ bonding mode. The two $Co^{III}$ ions are six-coordinate with octahedral geometries with an average $Co-L_{N,O}$ bond length of 1.916 (**4a**) and 1.911 (**4b**) Å. The two $Dy^{III}$ ions are eight coordinate with distorted square antiprismatic geometries with an average Dy−O bond length of 2.361 (**4a**) and 2.367 (**4b**) Å. The closest intermolecular Dy···Dy distance is 7.542 Å.

**Structural Comparisons.** While complexes **1−4** display subtle differences that distinguish each complex, the generic core structure is the same for all. Selected bond lengths and

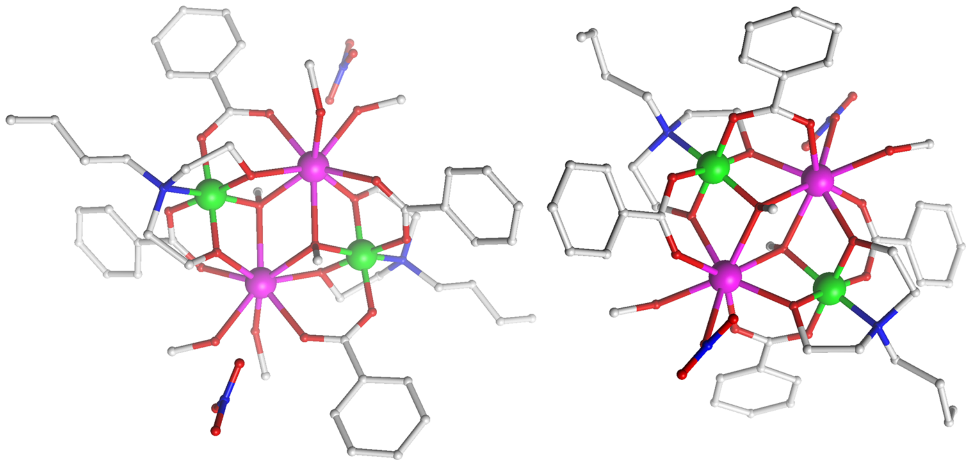

**Figure 3.** The molecular structure of **4a** (left) and **4b** (right) in the crystal. Disordered and H atoms are omitted for clarity. The color scheme is as in Figure 1.

**Table 2. Selected Bond Distances (Å) and Angles (deg) for Complexes 1−4**

| | 1a | 1b | 2 | 3 | 4a | 4b |
|---|---|---|---|---|---|---|
| Dy1−O1 | 2.441(7) | 2.480(7) | 2.423(11) | 2.433(3) | 2.426(5) | 2.384(5) |
| Dy1−O2 | 2.422(8) | 2.412(7) | 2.462(12) | 2.435(3) | 2.400(5) | 2.461(5) |
| Dy1−O3 | 2.324(7) | 2.331(7) | 2.359(9) | 2.339(3) | 2.333(4) | 2.346(4) |
| Dy1−O4 | 2.235(6) | 2.235(6) | 2.254(10) | 2.251(3) | 2.242(4) | 2.259(4) |
| Dy1−O5 | 2.448(6) | 2.435(6) | 2.413(10) | 2.401(3) | 2.450(4) | 2.456(4) |
| Dy1−O5′ | 2.428(6)$^{\mathrm{I}a}$ | 2.470(6)$^{\mathrm{II}a}$ | 2.447(9)$^{\mathrm{III}a}$ | 2.403(3)$^{\mathrm{IV}a}$ | 2.437(4)$^{\mathrm{V}a}$ | 2.413(4)$^{\mathrm{VI}a}$ |
| Dy1−O7′ | 2.281(6)$^{\mathrm{I}}$ | 2.270(6)$^{\mathrm{II}}$ | 2.249(10)$^{\mathrm{III}}$ | 2.245(3)$^{\mathrm{IV}}$ | 2.263(4)$^{\mathrm{V}}$ | 2.261(4)$^{\mathrm{VI}}$ |
| Dy1−O8′ | 2.341(6)$^{\mathrm{I}}$ | 2.322(7)$^{\mathrm{II}}$ | 2.349(10)$^{\mathrm{III}}$ | 2.340(3)$^{\mathrm{IV}}$ | 2.340(7)$^{\mathrm{V}}$ | 2.356(4)$^{\mathrm{VI}}$ |
| Co1−O4 | 1.891(7) | 1.896(7) | 1.889(10) | 1.893(3) | 1.879(4) | 1.864(4) |
| Co1−O5 | 1.929(6) | 1.927(6) | 1.940(10) | 1.939(3) | 1.934(4) | 1.935(4) |
| Co1−O7 | 1.890(6) | 1.876(6) | 1.881(10) | 1.894(3) | 1.873(4) | 1.877(5) |
| Co1−O9 | 1.924(7) | 1.952(6) | 1.937(10) | 1.914(3) | 1.918(4) | 1.896(4) |
| Co1−N1 | 1.964(8) | 1.964(7) | 1.945(11) | 1.961(4) | 1.983(5) | 1.981(6) |
| Co1−O10 | 1.896(7) | 1.905(6) | 1.964(10) | 1.918(3) | 1.914(4) | 1.910(4) |
| Dy1···Dy1′ | 4.075(7) | 4.088(6) | 4.026(10) | 3.998(6) | 4.103(6) | 4.077(6) |
| Dy1···Co1 | 3.2994(14) | 3.2796(14) | 3.253(2) | 3.257(6) | 3.2903(9) | 3.2691(9) |
| Dy1′···Co1 | 3.2829(13) | 3.2953(14) | 3.271(2) | 3.2684(8) | 3.2813(9) | 3.2916(9) |
| Dy1−O5−Dy1′ | 113.3(2) | 112.9(2) | 111.9(4) | 112.24(10) | 114.16(14) | 113.72(15) |

[a] Symmetry transformation: (I) −*x*, 1 − *y*, 2 − *z*; (II) 1/2 − *x*, 1/2 − *y*, 3/2 − *z*; (III) 2 − *x*, −*y*, −*z*; (IV) 1 − *x*, 1 − *y*, −*z*; (V) 1 − *x*, 1 − *y*, 1 − *z*; (VI) 2 − *x*, 1 − *y*, 1 − *z*.

angles for **1**−**4** are given in Table 2, following the labeling scheme shown in Figure 4.

Table 2 shows that the structural parameters vary little with regards to the bond lengths. An important consideration, however, known to influence the magnetic properties of lanthanide complexes at the single-ion level, is the coordination environment found around the Dy ion. Varying the type of ligand coordinated, as well as geometric distortions, all influence the splitting of the spin−orbit multiplets and, thus, the magnetic properties. Previously, we determined via dilution experiments, using the $\{\mathrm{Y^{III}Dy^{III}Co^{III}}_2\}$ complex,[7] that the slow relaxation of compound **1** was of single-ion origin, and thus alterations of the ligand and any distortions around the Dy$^{III}$ ion should affect the dynamic magnetic behavior. We have used the SHAPE software[20] to study the coordination polyhedra and determined that all of the Dy$^{III}$ ions in compounds **1**−**4** display distorted square antiprismatic geometries, with Continuous Shape Measures (CShMs) of 0.865, 0.923, 0.719, 1.686, 0.883, and 0.890 for Dy1 (**1**), Dy2 (**1**), **2**, **3**, Dy1(**4**), and Dy2(**4**), respectively. All Dy$^{III}$ ions show increased CShMs of between 2−4 for the next most closely related polyhedra, which are, in order of ascending CShMs: biaugmented trigonal prism, Johnson biaugmented trigonal prism, trigonal dodecahedron

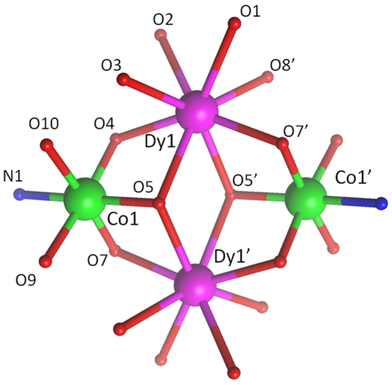

**Figure 4.** Labeled core structure for compounds **1**−**4**.

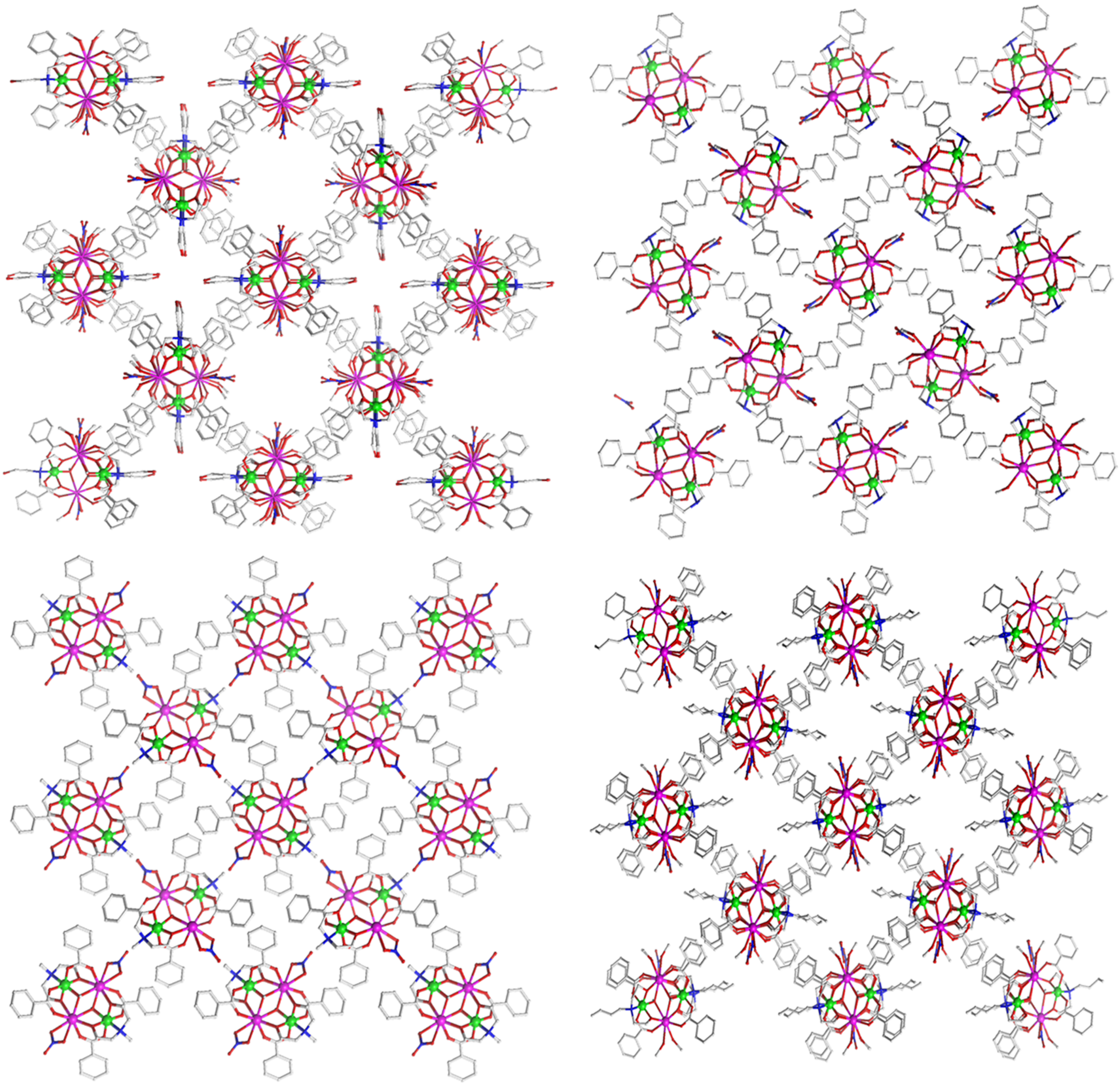

**Figure 5.** Comparison of the crystal packing for compounds **1** (top left), **2** (top right), **3** (bottom left), and **4** (bottom right). For each complex 1-D chains form perpendicular to the page, with compound **1** viewed along the *c*-axis, while **2**, **3**, and **4** viewed along the *a*-axis.

and snub disphenoid.[21] It is clear that compound **3** is the most distorted, with a CShM of almost double that of the others.

Comparing the crystal packing arrangements of **1**−**4** (Figure 5), we see that complex **1** (involving the $teaH_3$ ligand) packs in such a way that two types of channel are observed running along the crystallographic *c*-axis. These are formed via intermolecular H-bond interactions between the terminal MeOH and the coordinated/noncoordinated nitrate ions (Supporting Information, Figure S1), and edge-to-face aromatic C−H···$\pi$ interactions between the benzoate ligands (Supporting Information, Figure S2). Of the two channels present, the first contains the free, noncoordinating $teaH^{2-}$ arms, as well as disordered MeOH and $H_2O$ solvent molecules, while the second channel consists of disordered MeOH solvent molecules. Compound **2** ($deaH_2$) differs from **1**, overall. While there are still intermolecular H-bonded one-dimensional (1-D) chains running along the crystallographic *a*-axis via the MeOH and $NO_3^-$ ions, a third intermolecular H-bond forms between the N−H group of the $dea^{2-}$ ligand and the $NO_3^-$ counterion (Supporting Information, Figure S3, top), resulting in 3-D H-bonded sheets (Supporting Information, Figure S3, bottom). Further to this, the edge-to-face aromatic C−H···$\pi$ interactions between benzoate ligands are again present (Supporting Information, Figure S3, bottom). This results in the absence of any channels of the kind seen in **1**. Compound **3** displays no intermolecular H-bonds but packs in a near identical manner to that observed for **2**. This is likely to be driven by the aromatic interactions and the small methyl group on the diol ligand which does not sterically hinder the formation of this arrangement. For compound **4**, which contains the longer alkyl chain on the amine-polyol ligand, the packing motif is similar to that for **1**, and clearly differs from **2** and **3** due to the butyl group directing the packing. The arrangement seen in **4** still differs from **1**, however, which displays two types of channels; one channel has all four nonbonding protonated teaH$^{2-}$ arms all pointing toward each other, while the second is larger with just the terminal ligating groups on the Dy$^{III}$ ions directed into the space. For **4**, the larger butyl groups are sterically unable to do this, and thus the neighboring cluster rotates so that we now only observe one type of channel, with two butyl groups directed toward the center of the channel space.

**Magnetic Susceptibility Measurements.** The bulk magnetic properties of **1**−**4** were probed via variable temperature, dc and ac susceptibility measurements on polycrystalline samples. The dc studies (Figure 6) measured in magnetic fields of 0.1 and 1 T reveal room temperature $\chi_M T$ values at 1 T of 26.00, 28.79, 29.19, and 27.97 cm$^3$ K mol$^{-1}$, in good agreement with the expected value of 28.34 cm$^3$ K mol$^{-1}$ for two uncoupled Dy$^{III}$ ions. As the temperature is lowered, the $\chi_M T$ values decrease very gradually (300−50 K) before a much bigger decrease below 50 K, reaching values of 13.47, 14.37, and 15.43 and 14.48 cm$^3$ K mol$^{-1}$ at 0.1 T and 2 K for **1**−**4**, respectively. There is no field dependence in the range 70−2 K. It is noted that the decrease for compound **4** is more pronounced than for **1**−**3**. The decrease in $\chi_M T$ in all cases is due to the depopulation of the $m_J$ sublevels of the ground $J$ state, with the possibility of antiferromagnetic exchange/dipolar interactions also contributing to the behavior. The isothermal $M$ versus $H$ plots, shown in Supporting Information, Figure S4, each show sharp increases with increasing $H$, at low fields and low temperatures, with $M$ then increasing linearly at larger fields, reaching a value of 9.77, 10.86, 11.07, and 10.06 $N\beta$ at 2 K and 5 T, for **1**, **2**, **3**, and **4**, respectively. These values are lower than expected for the saturation value of two Dy$^{III}$ ions due to crystal field effects, which remove the degeneracy of the ground state.

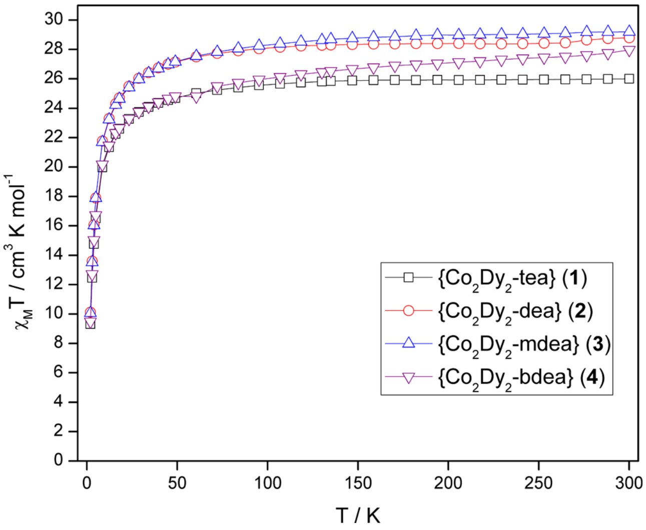

**Figure 6.** Plots of $\chi_M T$ vs $T$ for **1**−**4** measured at 1 T, the solid lines just join the points.

**Alternating Current Magnetic Susceptibility Measurements.** To probe the slow relaxation of the magnetization and quantum tunneling effects within these systems, variable temperature and frequency ac magnetic measurements were performed, utilizing a 3.5 Oe oscillating field and a zero-applied dc magnetic field. Both the in-phase ($\chi_M'$) (Supporting Information, Figure S5) and out-of-phase ($\chi_M''$) susceptibilities display a frequency (Figure 7) and temperature (Supporting Information, Figure S6) dependence below 20 K for **1**−**4**, signaling the blocking of the magnetization due to an anisotropy barrier.

Previously we reported a significant anisotropy barrier ($U_{eff}$) of 62 cm$^{-1}$ for compound **1**, with a pre-exponential factor of 5.64 × 10$^{-8}$ s ($R^2$ = 0.9974). It was also noted that **1** displayed a slower than usual quantum tunneling time compared to other lanthanide-based SMMs and was on the seconds time scale (>1.5 s).[7] Compounds **2**, **3**, and **4**, which also reveal features typical of SMM behavior, were no surprise, since each are closely related to **1**. The relaxation times at a given temperature derived from the ac experiments are plotted as ln($\tau$) versus 1/$T$ (Figure 8). From the frequency-dependent out-of-phase susceptibility behavior, it was found that the relaxation follows a thermally activated mechanism above 8.5, 10.5, 8.5, and 11 K for **1**−**4**, respectively, and plots of ln($\tau$) versus 1/$T$ are linear. These data were fitted to the Arrhenius law [$\tau = \tau_o \exp(U_{eff}/k_B T)$], which allowed for the evaluation of the anisotropy barrier and pre exponential factor. Each complex, as the temperature was lowered displayed a crossover to a temperature independent regime, as evidenced, first at intermediate temperatures by a curvature in the ln($\tau$) versus 1/$T$ plot, where thermal and quantum tunnelling mechanisms are active concurrently. The relaxation then becomes independent of temperature, indicative of a purely quantum tunnelling relaxation mechanism below <1.8, 2.2, 2.2, and 2 K, for **1**−**4**, respectively. The data points which are fitted to the regression line in the higher temperature region are taken to the largest R-squared value. At the point where this value drops off due to the curvature of the plot, these data are omitted from the Arrhenius analysis. Cole−Cole plots were also constructed ($\chi_M''$ vs $\chi_M'$) and fitted to a generalized Debye model (Supporting Information, Figure S7). It was generally found that each complex displayed a single relaxation mechanism in the thermally activated region, with a moderate distribution of relaxation times ($\alpha$). It must be noted however that compound **3** displayed the possibility of multiple relaxation modes, below 8 K, unfortunately there is not enough data to accurately model the dynamics for the second relaxation process. The resultant ac relaxation data are tabulated in Table 3.

The ln($\tau$) versus $T^{-1}$ plots show differences within the dynamic magnetic behavior for **1**−**4**. All display a thermally activated relaxation mechanism above 8.5 K, with a range of anisotropy barriers found, with values of 55 (**3**), 61 (**1**), 72 (**2**), and 80 cm$^{-1}$ (**4**). At low enough temperatures the QTM mechanism becomes faster than the thermally activated process and the relaxation time becomes independent of temperature. Differing characteristic $\tau_{QTM}$ times of 0.12 (**2**), 0.2 (**3**), 0.48 (**4**), and >1.5 s (**1**) are found, for each complex. Comparing the tunnelling times of the newly synthesized clusters **2**−**4**, to compound **1**, we see that pure quantum regimes occur at higher frequencies and thus faster time-scales than for **1**. More interestingly, it appears from the Cole−Cole data that compound **3** displays multiple relaxation pathways (Supporting Information, Figure S7) and this may relate to the greater level of distortion found around the Dy$^{III}$ ion, as determined via the SHAPE calculations (*vide supra*).

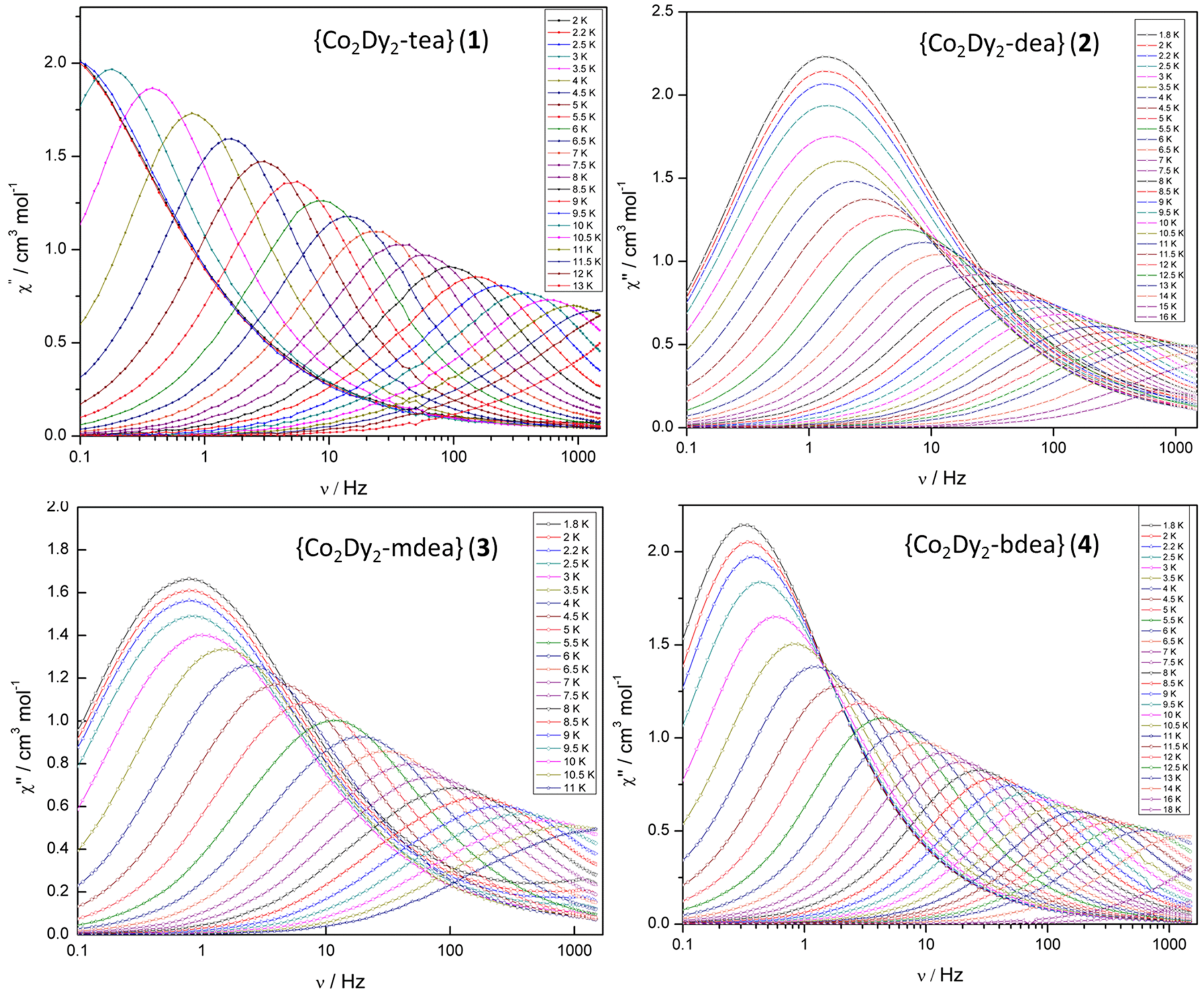

**Figure 7.** Frequency dependence of the out-of-phase ac susceptibilities, $\chi_M''$, of **1** (top, left), **2** (top right), **3** (bottom left), and **4** (bottom right).

We subsequently performed in-field ($H_{dc}$ = 1000 Oe) ac measurements on complex **1** to determine what effect the field has on the relaxation time. It was found that no shifts in the $\chi_M''(T)$ maxima were observed, and therefore no significant effect on the thermally activated relaxation time (Supporting Information, Figure S8).

Magnetic hysteresis measurements were performed using a conventional SQUID magnetometer on polycrystalline samples of **1**−**4**, to further study the relaxation dynamics. Unfortunately no open loops could be observed above 1.8 K (Supporting Information, Figure S9), with a large loss of magnetization at zero field. To gain any further insight on the magnetic relaxation and QTM then single crystal micro-Squid experiments at lower temperatures are required.

**Ab initio Calculations.** All calculations on complexes **1**−**4** were performed with the MOLCAS 7.8 program package[22] and were of the CASSCF/RASSI/SINGLE_ANISO type. To check the stability of the obtained solutions, two structural models for the mononuclear $Dy^{III}$ fragments have been employed: fragment **A** (small) and **B** (large). The structure of model **A** is shown in Supporting Information, Figure S10. Model **B** has the same structure as the initial $\{Co^{III}_2Dy^{III}_2\}$ complex, in which the neighboring Dy ion was computationally substituted by a diamagnetic Lu ion. The $Co^{III}$ ions were unaltered in all calculations. All atoms were described using standard basis sets from the ANO-RCC library available in Molcas.[23] The employed structures were both computed within two basis set approximations: *α*—small (DZP-quality) and *β*—large (TZP-quality). Supporting Information, Table S1 shows the contractions of the employed basis sets for all elements. To save disk space, the Cholesky decomposition of bielectronic integrals was employed with a threshold of $0.2 \times 10^{-7}$.[24] The spin-free wave functions and corresponding energies were calculated within the complete active space self-consistent field (CASSCF) method.[25] The active space of the CASSCF method included nine electrons in seven orbitals (4f orbitals of $Dy^{3+}$ ion). In view of the nonmagnetic ground state of both $Co^{III}$ ions, the entire $3d^6$ shells were kept in the inactive space (doubly occupied). Twenty-one sextet, 128 quartet, and 130 doublet states were further mixed by spin−orbit coupling using the RASSI program.[26] On the basis of the resulting spin−orbital multiplets, the SINGLE_ANISO program computed local magnetic properties (*g*-tensors, magnetic axes, magnetic susceptibilities, and magnetizations etc.).[8,27]

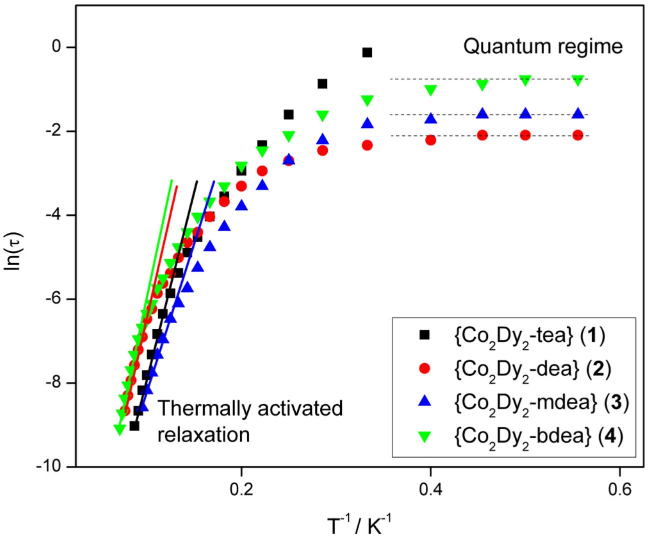

**Figure 8.** Plots of ln($\tau$) vs $T^{-1}$ for **1**−**4** under a zero applied dc field. The solid lines represent fits to the Arrhenius law of the thermally activated region; the dashed lines indicate the relaxation time of the temperature-independent relaxation mechanism.

The calculated electronic and magnetic properties of the individual Dy$^{III}$ free-ions for **1**−**4** show that the local *g*-tensors in the ground Kramers doublet are all strongly axial with a large $g_z$ value indicating a large magnetic moment, approaching that expected for a pure $m_J$ = $^{15}/_2$ state of $g_z$ = 20. This explains the presence of slow magnetic relaxation in all cases. The *g*-values of the first excited Kramers doublets for **1**−**4** are also strongly axial with values close to that expected for a pure $m_J$ = $^{13}/_2$ state of $g_z$ = 17.33. Higher energy Kramers doublets begin to deviate from axiality, signifying mixing of wave functions. The *g*-tensors of the most energetic states corresponding to the ground $^6H_{15/2}$ multiplet are also strongly axial, with $g_z$ values also approaching that expected for a pure $m_J$ = $^{15}/_2$ state, indicating the low symmetry of the crystal field, a feature that has been previously been examined.[13] The calculated energy gap between the ground Kramers doublet and the first two excited states with the associated *g* tensors are shown in Table 4. A complete list of the energies and *g* tensors for compounds **1**−**4** are given in the Supporting Information, Tables S2−S9. The orientations of the main anisotropy axes in the ground Kramers doublet for **1**−**4** are shown in Figure 9 (dashed lines). It is found that the direction of the main anisotropy axis does not lie along the pseudo 4-fold axis of the square antiprismatic geometry of each individual Dy ion. This has also been found to be the case in other recent Dy$^{III}$ examples.[28]

It was shown previously, via dilution studies, that the slow magnetic relaxation of **1** was of single-ion origin and, thus, the electronic and magnetic properties of the individual Dy$^{III}$ ions are of great importance.[7] Interestingly, it is found that the theoretically calculated lowest excitation energies of the individual Dy$^{III}$ ions correlate with the heights of the experimentally determined barriers in each complex. In this series of compounds, the experimental barrier of **4** (80 cm$^{-1}$) is largest followed by **2** (72 cm$^{-1}$) then **1** (61 cm$^{-1}$) and **3** (55 cm$^{-1}$), with the theoretically determined ground to first excited states found to be 112.2 (average of both sites), 108.3, 98.5 (average of both sites), and 87.5 cm$^{-1}$ for **4**, **2**, **1**, and **3**, respectively. We observe that the experimental relaxation barriers are systematically lower than the calculated energies of the first excited Kramers doublet on the Dy sites in **1**−**4**. This could be in part due to insufficient data in the high temperature (high frequency) domain (Figure 8), resulting in an underestimation of the slope of ln($\tau$) vs $T^{-1}$. Unfortunately we were unable to obtain these data due to the high frequency limit (1500 Hz) of our SQUID magnetometer. The observed barrier heights for each, however, suggest a strong relationship between the calculated ligand-field splitting and the experimentally determined thermally activated relaxation barriers. It should also be noted that the excitation energies of the Dy$^{III}$ sites on both individual molecules are close in energy at about 94−102 cm$^{-1}$, for **1**, and 104−119 cm$^{-1}$, for **4**, and this is consistent with the observation of a single thermally activated relaxation regime in the ac data.

The *ab initio* wave functions and energies for all Dy$^{III}$ sites in compounds **1**−**4** are employed in the computation of the intramolecular magnetic interactions. The exchange interaction is treated within the Lines model,[29] which describes the exchange coupling between the spin moments of magnetic sites in the absence of spin−orbit coupling by one parameter. In the case of spin orbit coupling, the projection of the Lines model accounts for anisotropic exchange interactions between metal sites. The Lines model is in fact exact in three limiting cases, with interactions between: (i) two isotropic (spin-only) magnetic centers (Heisenberg exchange); (ii) one isotropic and one strongly anisotropic center (Ising + Heisenberg = Ising exchange); (iii) two strongly anisotropic centers (Ising exchange). Equation 1 gives the Ising exchange Hamiltonian, where the anisotropic dipolar and exchange interactions are treated within the Lines model.[29]

$$H = -(J_{\text{dip}} + J_{\text{exch}})\hat{\tilde{s}}_{1,z}\hat{\tilde{s}}_{2,z} \tag{1}$$

where $\tilde{s}_{i,z}$ = (1)/(2) is the projection of the pseudospin corresponding to the lowest Kramers doublet of each ion onto the main anisotropy axis *z*. The dipolar contribution is considered exactly, while the exchange part is determined from a fit to the magnetic data. All calculations were performed using the POLY_ANISO routine.[30] The calculations reproduce the susceptibility and magnetization measurements well, with fits of the magnetic data shown Figures S11−S18 (Supporting Information). The exchange parameters obtained are summarized in Table 5.

The energies, corresponding tunnelling gaps and $g_Z$ values of the lowest four exchange doublet states of complexes **1**−**4** are given in Supporting Information, Tables S10− S13. It was found that the dipolar coupling is stronger than the exchange

**Table 3. Parameters Extracted from the ac Susceptibility Data**

| complex | $U_{\text{eff}}$ (cm$^{-1}$) | tunnelling frequency (Hz) | $\tau_{\text{QTM}}$ (s) | $\tau_{\text{O}}$ (s) | $\alpha$ |
|---|---|---|---|---|---|
| **1** | 61 ± 1 | <0.1 | >1.5 | 5.64 × 10$^{-8}$ | 0.29 (4 K)−0.24 (10.5 K) |
| **2** | 72 ± 2 | 1.29 | 0.12 | 6.05 × 10$^{-8}$ | 0.38 (1.8 K)−0.28 (12 K) |
| **3** | 55 ± 1 | 0.79 | 0.20 | 1.03 × 10$^{-7}$ | 0.42 (1.8 K)−0.30 (10.5 K) |
| **4** | 80 ± 1 | 0.34 | 0.48 | 3.38 × 10$^{-8}$ | 0.26 (1.8 K)−0.15 (14 K) |

**Table 4. Calculated Energy Spectrum of the Ground and Low-Lying Kramers Doublets and $g$-Tensors for Compounds 1−4**

| | doublet | energy (cm$^{-1}$) | $g_x$ | $g_y$ | $g_z$ | angle of $g_Z$ axis with the Dy−Dy direction[a] (in degrees) |
|---|---|---|---|---|---|---|
| compound **1**[b] | | | | | | |
| (molecule 1) | 1 | 0 | 0.022 | 0.033 | 19.697 | 84.7 |
| | 2 | 102.6 | 0.155 | 0.170 | 16.849 | |
| | 3 | 214.7 | 0.312 | 0.507 | 14.817 | |
| (molecule 2) | 1 | 0 | 0.021 | 0.029 | 19.717 | 84.5 |
| | 2 | 94.5 | 0.178 | 0.191 | 16.974 | |
| | 3 | 209.6 | 0.137 | 0.259 | 14.902 | |
| compound **2**[b] | | | | | | |
| | 1 | 0 | 0.005 | 0.005 | 19.839 | 89.9 |
| | 2 | 108.3 | 0.105 | 0.117 | 17.156 | |
| | 3 | 249.1 | 0.248 | 0.318 | 14.755 | |
| compound **3**[b] | | | | | | |
| | 1 | 0 | 0.011 | 0.012 | 19.859 | 89.7 |
| | 2 | 87.5 | 0.134 | 0.150 | 17.150 | |
| | 3 | 203.4 | 0.946 | 4.032 | 11.856 | |
| compound **4**[b] | | | | | | |
| (molecule 1) | 1 | 0 | 0.007 | 0.009 | 19.830 | 89.3 |
| | 2 | 119.9 | 0.125 | 0.141 | 17.139 | |
| | 3 | 262.0 | 0.223 | 0.290 | 14.569 | |
| (molecule 2) | 1 | 0 | 0.008 | 0.009 | 19.839 | 88.5 |
| | 2 | 104.6 | 0.137 | 0.183 | 17.076 | |
| | 3 | 230.2 | 1.475 | 2.240 | 13.360 | |

[a] The angle of the $g_Z$ axis is given relative to the Dy−Dy direction. Given that the molecules are centrosymmetric, the main anisotropy axes of the ground Kramers doublets of the Dy ions are parallel. Therefore, the intramolecular magnetic dipolar interaction is mainly defined by this angle. In particular, the fact that this angle is close to 90° for all investigated compounds, the intramolecular magnetic dipolar interaction stabilizes in the ground exchange state the antiferromagnetic arrangement of the magnetic moments on Dy ions. [b] Using model B and basis set $\beta$ (see Supporting Information for models).

coupling, as generally expected for Dy−Dy interactions. The dipolar interaction ($J_{\mathrm{dip}}$) is antiferromagnetic and dominant in all cases, while the exchange interaction ($J_{\mathrm{exch}}$) is antiferromagnetic in case of **1** and **2**, while it is found to be weakly ferromagnetic for **3** and **4**. The reason for the change in sign of the exchange parameters is likely due to small structural variations in the series. It is well-known that the exchange in lanthanides is more sensitive to structural changes than in TM complexes.[1] This, in all cases, leads to a nonmagnetic exchange ground state, with the first excited (magnetic) level lying ~1.45, ~1.33, ~1.25, and ~1.21 cm$^{-1}$ above the ground, for **1**−**4**, respectively. The next closest doublets are nonmagnetic and lie ~83−103, ~110, ~86 and ~100−120 cm$^{-1}$ above these, for **1**−**4**, respectively. It is found that the splitting of the ground and closest lying exchange doublets are all on the order of $10^{-6}$−$10^{-7}$ cm$^{-1}$, indicating that the QTM within each molecule will be relatively weak. This intrinsic tunnelling gap arises because of the non-Kramers nature of the coupled system. Another contribution that allows for QTM usually comes from the interaction with transverse magnetic fields that are induced by the magnetic moments of surrounding complexes; however, since the ground states are nonmagnetic due to the antiferromagnetic intracluster exchange, the magnetic field arising from surrounding complexes will diminish with lowering temperature. There is however another source of internal magnetic field, coming from the nuclear spins of constituent atoms, and also contributions from spin-phonon coupling which can be significantly different for the four complexes, explaining why the experimental data show slower QTM for **1** compared to **2**−**4** in the low-temperature region. On the other hand, for temperatures exceeding the exchange splitting in the complexes (Supporting Information, Tables S10−S13), that is, in the high temperature activated regime, when the thermal energy is still greater than the magnetic interaction, but still much lower than the first excited Kramers doublet on the Dy sites (Table 4). If the Arrenhius relaxation on individual sites is still not the dominant mechanism, then the relaxation via QTM on individual sites gives an important contribution.[14] The latter is defined by transversal components of the $g$ factors of the ground Kramers doublets on Dy sites ($g_x$ and $g_y$ in Table 4), which are largest for **1** among the four complexes. This nicely agrees with the experimental observation of the shortest relaxation time in the high-temperature domain being observed for this complex (Figure 8).

## ■ CONCLUSIONS

Building upon our original synthesis of a heterometallic $\{\mathrm{Co^{III}}_2\mathrm{Dy^{III}}_2\}$ butterfly type SMM, we have isolated three closely related complexes by means of various chemical modifications. We find that the three new derivatives all display SMM behavior but with subtly different dynamic magnetic properties. Each complex displayed a unique anisotropy barrier, with values ranging from 55 to 80 cm$^{-1}$. Previous studies had revealed that the slow relaxation of the magnetization was of single ion in origin.[7] The variation in barrier height was thus determined to be a consequence of the unique coordination and geometric environments observed around the Dy$^{\mathrm{III}}$ ions of each complex, which as determined from *ab initio* calculations influences the crystal field split lowest excitation energies of the individual Dy$^{\mathrm{III}}$ ions. It was found that there was a strong correlation formed between the heights of the theoretically calculated energy gaps between the ground and first excited states and the experimentally observed anisotropy barriers. Each complex also displayed a unique characteristic tunnelling

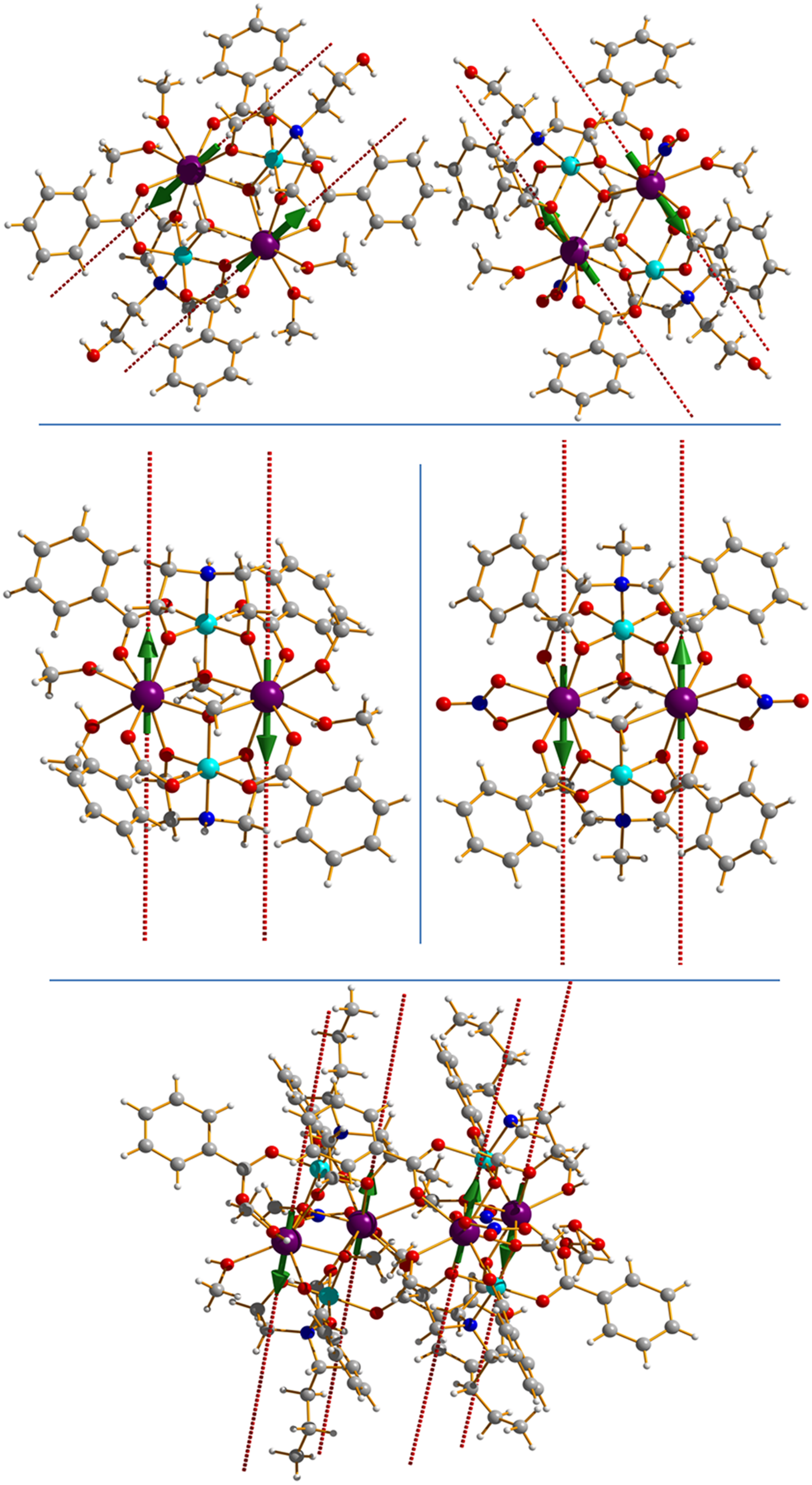

**Figure 9.** Orientations of the local magnetic moments in the ground doublet of complexes **1** (top), **2** (middle, left) **3** (middle, right), and **4** (bottom). Green arrows show the antiferromagnetic coupling of the local magnetic moments of the Dy ions in the ground state.

time, of between 0.1 and >1.5 s, relatively slow for lanthanide-based SMMs.[12] The magnetic exchange between the $Dy^{III}$ ions revealed overall antiferromagnetic interactions for each compound, derived from the dominant dipolar exchange

**Table 5. Exchange Interactions between the Dy Ions in 1−4 ($cm^{-1}$)**

| | model[a] | $J_{dip}$[b] | $J_{exch}$ | $J_{total} = J_{dip}$[b] $+ J_{exch}$ |
|---|---|---|---|---|
| **Compound 1** | | | | |
| *molecule 1* | A$\alpha$ | −2.301 78 | −0.619 50 | −2.921 28 |
| | A$\beta$ | −2.398 94 | −0.536 25 | −2.935 19 |
| | B$\alpha$ | −2.300 06 | −0.621 00 | −2.921 06 |
| | B$\beta$ | −2.397 14 | −0.539 75 | −2.936 89 |
| *molecule 2* | A$\alpha$ | −2.414 88 | −0.518 50 | −2.933 38 |
| | A$\beta$ | −2.418 17 | −0.539 00 | −2.957 17 |
| | B$\alpha$ | −2.416 85 | −0.520 50 | −2.937 35 |
| | B$\beta$ | −2.419 68 | −0.539 25 | −2.958 93 |
| **Compound 2** | | | | |
| | B$\alpha$ | −2.611 84 | −0.039 50 | −2.770 75 |
| | B$\beta$ | −2.610 73 | −0.042 75 | −2.774 25 |
| **Compound 3** | | | | |
| | B$\alpha$ | −2.690 86 | 0.184 25 | −2.626 25 |
| | B$\beta$ | −2.691 57 | 0.190 25 | −2.620 50 |
| **Compound 4** | | | | |
| *molecule 1* | B$\alpha$ | −2.468 31 | 0.042 25 | −2.540 75 |
| | B$\beta$ | −2.464 78 | 0.053 00 | −2.529 75 |
| *molecule 2* | B$\alpha$ | −2.508 51 | 0.056 75 | −2.567 56 |
| | B$\beta$ | −2.509 71 | 0.071 50 | −2.555 75 |

[a] See Supporting Information, Table S1 for models and basis sets. [b] Contribution only from the Ising terms $\sim\hat{s}_{1,z}\hat{s}_{2,z}$. In the calculation of the exchange spectrum (Supporting Information, Tables S10 and S13) the dipolar interaction included all terms.

resulting in a nonmagnetic ground states for **1−4**. The diamagnetic ground states coupled with the small tunnelling gaps are the reason for the slower than commonly observed quantum tunnelling time scales, under zero applied magnetic dc field. In a general sense, this study shows that the SMM properties can be fine-tuned via simple substitution of ligands around the magnetic centers, as well as tailoring the properties via chemical modifications to peripheral ligands not directly associated with the magnetic core.

## ■ ASSOCIATED CONTENT

### Ⓢ Supporting Information

Crystallographic data in cif format; Figures S1−S3 packing diagrams and H-bonding interactions; Figure S4, isothermal magnetization plots; Figure S5−S8, ac susceptibility plots; Figure S9, Magnetic hysteresis plot; Figure S10, structure of fragment A in **1**; Figures S11−S14, measured and calculated $\chi_M T$ data; Figures S15−S18, measured and calculated molar magnetizations versus field; Table S1, basis sets employed in *ab initio* calculations; Table S2, energies of lowest Kramers doublets; Table S3−S9, energies of lowest Kramers doublets and *g*-tensors; Table S10−S13, energies, $g_z$ values, and tunnelling gaps of lowest exchange doublets.This material is available free of charge via the Internet at http://pubs.acs.org. CCDC numbers for **1−4**, 885502, 945543, 945544, 945545. These data can be obtained free of charge from the Cambridge Crystallographic Data Centre via www.ccdc.cam.ac.uk/data_request/cif.

## ■ AUTHOR INFORMATION

### Corresponding Authors

*E-mail: keith.murray@monash.edu. (K.S.M.)
*E-mail: Liviu.Chibotaru@chem.kuleuven.be. (L.F.C.)

### Notes

The authors declare no competing financial interest.

## ■ ACKNOWLEDGMENTS

K.S.M. thanks the Australian Research Council (ARC) and the Australia-India Strategic Research Fund (AISRF) for support of this work. L.C. and L.U. acknowledge the support of the Flemish Science Foundation (FWO) and of INPAC and Methusalem programs of the University of Leuven. N.F.C. thanks The University of Manchester for a President's Doctoral Scholarship. Structural aspects of this research were undertaken on the MX1 beamline at the Australian Synchrotron, Clayton, Victoria, Australia.

## ■ REFERENCES

(1) (a) Christou, G.; Gatteschi, D.; Hendrikson, D. N.; Sessoli, R. *MRS Bull.* **2000**, 725. (b) Woodruff, D. N.; Layfield, R. A.; Winpenny, R. E. P. *Chem. Soc. Rev.* **2013**, *113*, 5110.

(2) (a) Leuenberger, M. N.; Loss, D. *Nature* **2001**, *410*, 789. (b) Bogani, L.; Wernsdorfer, W. *Nat. Mater.* **2008**, *7*, 179. (c) Vincent, R.; Klyatskaya, S.; Ruben, M.; Wernsdorfer, W.; Balestro, F. *Nature* **2012**, *488*, 357. (d) Van Der Zant, H. S. J. *Nat. Nanotechnol.* **2012**, *7*, 555. (e) Wernsdorfer, W. *Nat. Nanotechnol.* **2009**, *4*, 145. (f) Urdampilleta, M.; Klyatskaya, S.; Cleuziou, J.-P.; Ruben, M.; Wernsdorfer, W. *Nat. Mater.* **2011**, *10*, 502.

(3) Aromi, G.; Brechin, E. K. *Struct. Bonding (Berlin, Ger.)* **2006**, *122*, 1.

(4) Ishikawa, N.; Sugita, M.; Ishikawa, T.; Koshihara, S.; Kaizu, Y. *J. Am. Chem. Soc.* **2003**, *125*, 8694.

(5) (a) Ganivet, C. R.; Ballesteros, B.; de la Torre, G.; Clemente-Juan, J. M.; Coronado, E.; Torres, T. *Chem.—Eur. J.* **2013**, *19*, 1457. (b) Blagg, R. J.; Muryn, C. A.; McInnes, E. J. L.; Tuna, F.; Winpenny, R. E. P. *Angew. Chem., Int. Ed.* **2011**, *50*, 6530. (c) Blagg, R. J.; Tuna, F.; McInnes, E. J. L.; Winpenny, R. E. P. *Chem. Commun.* **2011**, *47*, 10587. (d) Hewitt, I. J.; Tang, J.; Madhu, N. T.; Anson, C. E.; Lan, Y.; Luzon, J.; Etienne, M.; Sessoli, S.; Powell, A. K. *Angew. Chem., Int. Ed.* **2010**, *49*, 1. (e) Rhinehart, J. D.; Fang, M.; Evans, W. J.; Long, J. R. *Nat. Chem.* **2011**, *3*, 538. (f) Rhinehart, J. D.; Fang, M.; Evans, W. J.; Long, J. R. *J. Am. Chem. Soc.* **2011**, *133*, 14236.

(6) (a) Ungur, L.; Van den Heuvel, W.; Chibotaru, L. F. *New J. Chem.* **2009**, *33*, 1224. (b) Ungur, L.; Langley, S. K.; Hooper, T.; Moubaraki, B.; Brechin, E. K.; Murray, K. S.; Chibotaru, L. F. *J. Am. Chem. Soc.* **2012**, *134*, 18554.

(7) Langley, S. K.; Chilton, N. F.; Ungur, L.; Moubaraki, B.; Chibotaru, L.; Murray, K. S. *Inorg. Chem.* **2012**, *51*, 11873.

(8) Chibotaru, L. F.; Ungur, L. *J. Chem. Phys.* **2012**, *137*, 064112.

(9) Boulon, M.-E.; Cucinotta, G.; Liu, S.-S; Jiang, S.-D.; Ungur, L.; Chibotaru, L.; Gao, S.; Sessoli, R. *Chem.—Eur. J.* **2013**, *19*, 13726.

(10) Liu, J.-L.; Chen, Y.-C.; Zheng, Y.-Z.; Lin, W.-Q.; Ungur, L.; Wernsdorfer, W.; Chibotaru, L. F.; Tong, M.-L. *Chem. Sci.* **2013**, *4*, 3310.

(11) Blagg, R. J.; Ungur, L.; Tuna, F.; Speak, J.; Comar, P.; Collison, D.; Wernsdorfer, W.; McInnes, E. J. L.; Chibotaru, L. F.; Winpenny, R. E. P. *Nat. Chem.* **2013**, *5*, 673.

(12) Guo, Y.-N.; Xu, G.-F.; Wernsdorfer, W.; Ungur, L.; Guo, Y.; Tang, J.; Zhang, H.-J.; Chibotaru, L. F.; Powell, A. K. *J. Am. Chem. Soc.* **2011**, *133*, 11948.

(13) Ungur, L.; Chibotaru, L. F. *Phys. Chem. Chem. Phys.* **2011**, *13*, 20086.

(14) Feltham, H. L. C.; Lan, Y.; Klöwer, F.; Ungur, L.; Chibotaru, L. F.; Powell, A. K.; Brooker, S. *Chem.—Eur. J.* **2011**, *17*, 4362.

(15) Ungur, L.; Thewissen, M.; Costes, J.-P.; Wernsdorfer, W.; Chibotaru, L. F. *Inorg. Chem.* **2013**, *52*, 6328.

(16) McPhillips, T. M.; McPhillips, S. E.; Chiu, H. J.; Cohen, A. E.; Deacon, A. M.; Ellis, P. J.; Garman, E.; Gonzalez, A.; Sauter, N. K.; Phizackerley, R. P.; Soltis, S. M.; Kuhn, P. *J. Synchrotron Radiat.* **2002**, *9*, 401.

(17) Kabsch, W. *J. Appl. Crystallogr.* **1993**, *26*, 795.

(18) Sheldrick, G. M. *Acta Crystallogr., Sect. A* **2008**, *A64*, 112.

(19) (a) Powell, A. K.; Heath, S. L.; Gatteschi, D.; Pardi, L.; Sessoli, R.; Spina, G.; Del Giallo, F.; Pieralli, F. *J. Am. Chem. Soc.* **1995**, *117*, 2491. (b) Goodwin, J. C.; Sessoli, R.; Gatteschi, D.; Wernsdorfer, W.; Powell, A. K.; Heath, S. L. *J. Chem. Soc., Dalton Trans.* **2000**, 1835.

(20) (a) Alvarez, S.; Alemany, P.; Casanova, D.; Cirera, J.; Llunell, M.; Avnir, D. *Coord. Chem. Rev.* **2005**, *249*, 1693. (b) Cirera, J.; Ruiz, E.; Alvarez, S. *Organometallics* **2005**, *24*, 1556.

(21) Casanova, C.; Llunell, M.; Alemany, P.; Alvarez, S. *Chem.—Eur. J.* **2005**, *11*, 1479.

(22) Aquilante, F.; De Vico, L.; Ferre, N.; Ghigo, G.; Malmqvist, P. Å.; Neogrady, P.; Pedersen, T. B.; Pitonak, M.; Reiher, M.; Roos, B. O.; Serrano-Andres, L.; Urban, M.; Veryazov, V.; Lindh, R. *J. Comput. Chem.* **2010**, *31*, 224.

(23) Roos, B. O.; Lindh, R.; Malmqvist, P.-Å.; Veryazov, V.; Widmark, P.-O. *J. Phys. Chem. A* **2005**, *109*, 6575.

(24) Koch, H.; de Meras, A. S.; Pedersen, T. B. *J. Chem. Phys.* **2003**, *118*, 9481.

(25) Roos, B. O.; Taylor, P. R.; Siegbahn, P. E. *Chem. Phys.* **1980**, *48*, 157.

(26) Roos, B. O.; Malmqvist, P.-A. *Phys. Chem. Chem. Phys.* **2004**, *6*, 2919.

(27) Ungur, L., Chibotaru, L. F. *SINGLE_ANISO module in MOLCAS*: http://www.molcas.org/documentation/manual/node95.html.

(28) (a) Cucinotta, G.; Perfetti, M.; Luzon, J.; Etienne, M.; Carr, P. E.; Caneschi, A.; Calvez, G.; Bernot, K.; Sessoli, R. *Angew. Chem., Int. Ed.* **2012**, *51*, 1606. (b) Boulon, M.-E.; Cucinotta, G.; Luzon, J.; Degl'Innocenti, C.; Perfetti, M.; Bernot, K.; Calvez, G.; Caneschi, A.; Sessoli, R. *Angew. Chem., Int. Ed.* **2013**, *52*, 350. (c) Chilton, N. F.; Langley, S. K.; Moubaraki, B.; Soncini, A.; Batten, S. R.; Murray, K. S. *Chem. Sci.* **2013**, *4*, 1719.

(29) Lines, M. E. *J. Chem. Phys.* **1971**, *55*, 2977.

(30) Ungur, L.; Chibotaru, L. F. *POLY_ANISO* program; KU Leuven: Belgium, 2007.